


 Cite this: *RSC Adv.*, 2022, **12**, 7835

## Efficacy of surface-functionalized $Mg_{1-x}Co_xFe_2O_4$ ( $0 \leq x \leq 1$ ; $\Delta x = 0.1$ ) for hyperthermia and *in vivo* MR imaging as a contrast agent<sup>†</sup>

 M. Aminul Islam, <sup>abc</sup> M. Razibul Hasan,<sup>a</sup> M. Mahbubabul Haque,<sup>a</sup> Rimi Rashid,<sup>a</sup> Ishaque M. Syed<sup>c</sup> and S. Manjura Hoque <sup>\*a</sup>

Surface-functionalized  $Mg_{1-x}Co_xFe_2O_4$  ( $0 \leq x \leq 1$ ;  $\Delta x = 0.1$ ) can be an exciting candidate as an MRI contrast agent and for thermotherapeutic applications. The figure-of-merit,  $T_2$ , relaxivity,  $r_2$ , of MRI and specific loss power, SLP, of hyperthermia depend on the structural and magnetic properties of the nanoparticles. We synthesized cobalt-substituted magnesium ferrite  $Mg_{1-x}Co_xFe_2O_4$  ( $0 \leq x \leq 1$  with  $\Delta x = 0.1$ ) nanoparticles using a chemical co-precipitation method. The lattice parameter and average crystallite size increase with the increase in cobalt content. The force-constant of FTIR of the tetrahedral sites increases, and that of the octahedral sites decreases with an increase in cobalt content. The room temperature Mössbauer spectra of  $Mg_{1-x}Co_xFe_2O_4$  show that the Mössbauer absorption area of the A site decreases, and the Mössbauer absorption area of the B site increases with  $x$ . The Mössbauer spectra and  $M-H$  hysteresis loops at room temperature confirmed that a transition from fast relaxation (superparamagnetic) to mixed slow/fast (superparamagnetic/ferrimagnetic) relaxation occurs with changing cobalt content. The cobalt ion tends to occupy the octahedral B site, which makes the A-B interaction stronger; therefore, we see the above transition. Cytotoxicity experiments on HeLa cells revealed that both chitosan and chitosan-coated magnesium cobalt ferrite nanoparticles are biocompatible. In the  $Mg_{1-x}Co_xFe_2O_4$  series, both  $r_2$  and SLP increase with  $x$  because of the increase in magnetization and anisotropy.

Received 5th February 2022

Accepted 10th February 2022

DOI: 10.1039/d2ra00768a

[rsc.li/rsc-advances](http://rsc.li/rsc-advances)

## Introduction

Multifunctional superparamagnetic spinel ferrite nanoparticles, smaller than many biological objects in size, are suitable for numerous applications such as MRI contrast dyes, tissue repair, immunoassays, detoxification of body fluids, hyperthermia, drug delivery, and cell separation.<sup>1-6</sup> To date, these nanoparticles are of great importance for molecular-level detection and therapy. There is ample information on the effects of size, shape, and homogeneity of nanoparticles for colloidal suspensions. Amplifying the magnetic and physical properties relies on the composition of the nanoparticles in the first place. For most practical purposes, the size of the nanoparticles is in the range of  $<20$  nm,<sup>3,7</sup> which causes the nanoparticles to have a large surface area, and they are highly surface-active due to their smaller size. This phenomenon provides massive scope for surface modification to achieve targeted delivery and biocompatibility. Coating

materials that modify the surfaces of nanoparticles can be organic polymers (dextran, chitosan, polyethylene glycol, polysorbate, polyaniline, *etc.*), organic surfactants (sodium oleate, dodecylamine, *etc.*), inorganic materials (gold, silica, carbon, *etc.*), and bioactive molecules (liposomes, peptides, ligands, *etc.*).<sup>8-11</sup> We investigated samples coated with biocompatible chitosan and PEG to reduce their toxic effects in our previous studies.<sup>12-14</sup> Surface modifications by coating and control of the size, shape, pH, surface charge, and hydrodynamic diameter allow an efficient method of controlling the significant parameters necessary for biomedical applications. Particularly for biomagnetic applications, the requirement of higher magnetic moments at smaller particle sizes with uniform physical and chemical properties is crucial.

Magnetic fluid hyperthermia (MFH) has drawn considerable attention in cancer treatment with radio frequency (rf) magnetic fields for localized heating mediated by magnetic nanoparticles. Regarding the magnetic fluid-based localized hyperthermia, the temperature of the tumor rises to 42–46 °C with an application of an rf magnetic field for 30–60 minutes. The heat thus generated causes the damage or weakening of the cancerous tissue. Blood vessels inside the tumor and cancerous tissues are porous due to the disordered formation. It helps to gather nanoparticles inside the malignant tissue, which results in

<sup>a</sup>Materials Science Division, Atomic Energy Centre Dhaka, Bangladesh Atomic Energy Commission, 1000, Dhaka, Bangladesh. E-mail: manjura\_hoque@yahoo.com

<sup>b</sup>Magura Govt. Mahila College, Magura, Bangladesh

<sup>c</sup>Department of Physics, University of Dhaka, Bangladesh

† Electronic supplementary information (ESI) available. See DOI: 10.1039/d2ra00768a



localized heating in the malignant cells. Thus, it causes damage to localized or deeply-seated tumors. Magnetic fluid hyperthermia is advantageous compared to another magnetic thermotherapy such as thermoablation. In the thermoablation process, the temperature of the cancerous cells goes up to 56 °C for a short period. High temperature in thermoablation may cause widespread necrosis, coagulation, and carbonization of the cancerous tissue.<sup>15–17</sup>

$\text{MgFe}_2\text{O}_4$  nanoparticles are composed of bio-compatible Mg and Fe, which are nontoxic atoms. Inadvertently, magnesium ferrite shows low magnetic moment, zero coercivity, and zero retentivity because nonmagnetic  $\text{Mg}^{2+}$  has the tendency to occupy B sites<sup>17,18</sup> and therefore, the withdrawal of the magnetic field would demagnetize the nanoparticles faster, which is plausible for biomedical applications. Further, the average daily intake of cobalt is 5 to 60 mg per day<sup>19</sup> and for Mg, it is 420 mg per day.<sup>20</sup> Therefore, reference daily intake magnesium is about  $10^4$  times higher than cobalt. On the other hand,  $\text{CoFe}_2\text{O}_4$  nanoparticles have a high magnetic moment and anisotropy, which generates more heat in an alternating magnetic field, which makes them suitable for localized hyperthermia.<sup>21–23</sup> The substitution of magnesium by cobalt enhances specific loss power through Néel's and Brownian relaxation, and the hysteresis loss of nanoparticles. We replaced magnesium with cobalt in the entire spectrum of  $\text{Mg}_{1-x}\text{Co}_x\text{Fe}_2\text{O}_4$  with  $\Delta x = 0.1$  to obtain the compositions, which exploits the positive attributes of both  $\text{MgFe}_2\text{O}_4$  and  $\text{CoFe}_2\text{O}_4$  to deliver higher efficacy and biocompatibility for local magnetic hyperthermia treatment and MRI contrast dye.

Magnetic resonance imaging (MRI) is the most influential diagnostic tool for imaging the brain and central nervous system and the soft tissue of humans, evaluating the cardiac function, and identifying tumors. Various magnetic nanoparticles as MRI contrast agents due to their novel properties, such as small size, large surface area, high magnetic moment, and zero or negligible coercivity, are in use. MRI contrast enhancement occurs due to interaction between the contrast agent and the adjacent water protons influenced by the particle size, magnetic moment, anisotropy constant. Magnetic nanoparticles with high crystallinity are potential candidates as  $T_2$  MRI contrast agents.<sup>24–30</sup> Superparamagnetic gadolinium-based nanoparticles are in frequent use as contrast agents in hospital MRI, which has the disadvantage of weakening the kidneys. For many applications, especially for the detection of malignant tissues, MRI becomes irrelevant without a contrast agent. In spite of plentiful research on ferrite nanoparticles as MRI contrast agents, finding a suitable composition that is biocompatible still remains an open question. Therefore, another purpose of this study is to observe the ramifications of  $\text{Mg}_{1-x}\text{Co}_x\text{Fe}_2\text{O}_4$  as an MRI contrast-enhancing dye.

## Materials and methods

### Sample preparation

We synthesized a series of  $\text{Mg}_{1-x}\text{Co}_x\text{Fe}_2\text{O}_4$  ( $0 \leq x \leq 1$  with  $\Delta x = 0.1$ ) by wet chemical coprecipitation method using NaOH the coprecipitating agent. Analytical grade of  $\text{Mg}(\text{NO}_3)_2 \cdot 6\text{H}_2\text{O}$ ,

$\text{CoCl}_2 \cdot 6\text{H}_2\text{O}$ , and  $\text{FeCl}_3$  were mixed in the required molar ratio and 8 M of NaOH solution was added dropwise under continuous stirring using a magnetic stirrer at a speed of 400 rpm. Extra NaOH was added dropwise to maintain the pH of the solution to a value of 11–13. The mixture was heated to 353 K for one hour to complete the reaction and was retained at room temperature. The excess NaOH was washed out from the mixture by centrifugation at 13 000 rpm ten times. The  $\text{AgNO}_3$  test confirmed the removal of NaOH. Then, the particles were dried at 343 K for 72 h to complete the ferritization reaction. Finally, we ground the dried nanoparticles in an agate mortar-pestle for further functionalization.

### Coating

We prepared 2% chitosan solution by adding 2 g chitosan in 100 mL de-ionized water under continuous stirring at 400 rpm using a magnetic stirrer for 72 hours. A required amount of acetic acid was added to the solution to dissolve chitosan in water. Then, the solution was centrifuged two times at 13 000 rpm to remove any undissolved chitosan. We added 20 mg of  $\text{Mg}_{1-x}\text{Co}_x\text{Fe}_2\text{O}_4$  ( $0 \leq x \leq 1$  with  $\Delta x = 0.1$ ) particles to 1 mL of 2% chitosan solution, followed by vortex and sonication several times to get 20 mg  $\text{mL}^{-1}$  chitosan-coated Mg–Co nanoparticles as the stock solution. Finally, we prepared other concentrations by diluting the stock solution.

### Characterization

We conducted the structural characterization of the as-synthesized  $\text{Mg}_{1-x}\text{Co}_x\text{Fe}_2\text{O}_4$  ( $0 \leq x \leq 1$  with  $\Delta x = 0.1$ ) nanoparticles by an X-ray diffractometer (XRD), (Model: PW 3040-X'Pert PRO PANalytical, Philips, Netherlands) at 40 kV and 30 mA. The range of  $2\theta$  angle was 15–70° using  $\text{CuK}_\alpha$  radiation ( $\lambda = 1.54059 \text{ \AA}$ ) with a scan step size of 0.0167°. We carried out transmission electron microscopy studies using a TALOS 200X, ThermoFisher, USA, with an operating voltage of 200 kV. For TEM analysis, we dispersed the samples in ethanol and drop-cast them on an electron-transparent carbon-coated Cu grid, followed by drying. The bare samples were in the solid state and the coated samples were in the liquid state. Mössbauer spectroscopy was performed using a model: 302 SEE Co., USA, gamma ray resonant spectrometer having a transmission geometry and constant acceleration mode with a transducer velocity of 11  $\text{mm s}^{-1}$ . Before starting the measurement, the spectrometer was calibrated using a metallic iron foil as the standard sample, and zero velocity was considered as the centroid of the Mössbauer spectrum. The Mössbauer data were acquired at room temperature, zero magnetic fields, and the acquisition time of 72 hours. The FTIR measurements were carried out by an FTIR spectrometer, model: L1600300 Spectrum PerkinElmer, United Kingdom with the attenuated total reflection (ATR) attachment. The sample in a small amount was placed on the diamond/ZnSe crystal of ATR using a pressure arm, which allows good contact of the sample with the crystal. The FTIR spectra of chitosan, bare, and chitosan-coated magnesium cobalt ferrite nanoparticles were acquired in the range of 350–3000  $\text{cm}^{-1}$ . The Raman Spectroscopy



measurements were carried out using a CRS+ 500/BX53, Monovista, S & I Spectroscopy & Imaging, Germany. A diode Laser System of 785 nm was used, which was internally mounted by 100 mW, and the Laser line cleaned up with edge filter width  $\leq 60 \text{ cm}^{-1}$ . Raman spectra were acquired for pelletized samples in the range from 200 to  $3500 \text{ cm}^{-1}$ . The samples' hydrodynamic size and zeta potential were investigated by a dynamic light scattering (DLS) instrument, model: ZEN 3600, Zetasizer, Malvern, U.K. The hydrodynamic size of the chitosan-coated nanoparticles was acquired at 25 °C, 37 °C, and 44 °C. The magnetizations at room temperature of all the samples were measured by the Physical Property Measurement (PPMS) System, model: 10307, Quantum Inc., USA. The *M-H* hysteresis loops of all the samples were measured from -5 to +5 Tesla in the bare and coated state.

### Cytotoxic assay

We carried out the cytotoxic assay on the HeLa cell line by a Bio Safety Cabinet, Model: NU-400 E, Nuaire, U.S.A, CO<sub>2</sub> Incubator (Nuaire, U.S.A), Hemocytometer, Optika, Italy, and an inverted light microscope. The media used was DMEM (Dulbecco's Modified Eagles' Medium) containing 1% penicillin-streptomycin (11), 0.2% gentamycin, and 10% fetal bovine serum (FBS). HeLa cells ( $4 \times 10^5$  per 200  $\mu\text{L}$ ) were seeded in 96-well plates and incubated for 24 hours in a CO<sub>2</sub> incubator containing 37 °C temperature and 5% CO<sub>2</sub>. Then, they were filtered (using 0.45  $\mu\text{m}$  syringe filter) 50  $\mu\text{L}$  of uncoated and coated Mg<sub>1-x</sub>Co<sub>x</sub>Fe<sub>2</sub>O<sub>4</sub> ( $0 \leq x \leq 1$  with  $\Delta x = 0.1$ ) nanoparticles with the concentration of 4 mg mL<sup>-1</sup> were added in each well. Duplicate wells were used for each sample. After 48 hours of incubation, insoluble samples were washed out several times with media. The survival of the cells was investigated by cell counting using a hemocytometer and an inverted light microscope using the following equations.

Cell viability was studied manually by a hemocytometer as,

$$\% \text{ cell viability} = \frac{\text{Total viable cells (unstained)}}{\text{Total cells (viable + dead)}} \times 100 \quad (1)$$

where, viable cells (per mL) = average viable cell count per square  $\times$  dilution factor of 10<sup>4</sup>; average viable cells (count per square) = (total number of viable cells in 4 squares)/4; dilution factors = (volume of sample + volume of diluting liquid)/volume of samples.

### Hyperthermia studies

We investigated the hyperthermia properties by a hyperthermia setup, model: EASY HEAT 5060LI, Ambrell, U.S.A. The hyperthermia setup consists of a sample coil of 8 turns that has a diameter of 4 cm. During the hyperthermia experiment, the current passing through the rf coil was 283 A, and the frequency was 343 kHz, which generated an rf magnetic field of 26 mT. The volume of the chitosan-coated solution was 600  $\mu\text{L}$ , and the concentration was 0.5, 1, 2, and 4 mg mL<sup>-1</sup>. An Eppendorf tube containing the solution was placed inside the rf coil for induction heating for different time intervals at a 26 mT magnetic field. We measured the temperature using an optical

fiber thermometer. The following equation yielded the specific loss power (SLP).

$$\text{SLP} = \frac{c}{m} \frac{dT}{dt} \quad (2)$$

*C* is the heat capacity of the solution, and *m* is the relative mass of the magnetic nanoparticles. The slope of the linear range of temperature *vs.* time curves provided  $\Delta T/\Delta t$ . The concentration of the magnetic nanoparticle is small, and therefore we considered the heat capacity of water to be 4.18 J g<sup>-1</sup> K<sup>-1</sup> for the sample.<sup>22,31</sup>

### Magnetic resonance imaging

We acquired phantom images containing chitosan-coated nanoparticles. The *T*<sub>2</sub> weighted fast spin-echo (FSE) MR images were acquired using the machine of model: MRS7017, MR solution, United Kingdom. During imaging, the repetition time (TR) was 4000 ms, slice thick-ness (THK) was 1.0 mm, and FOV was 40  $\times$  40. We acquired *T*<sub>2</sub> mapping with several echo times (TE) of 7, 14, 21, 28, 35, 42, 49, 56, 63, 70, 77, 84, 91, 98, 105, and 112 ms. Eleven phantoms were prepared by filling small Eppendorf tubes with five different concentrations of 0.04, 0.1, 0.2, 0.3, and 0.4 mM for each cobalt content *x* of Mg<sub>1-x</sub>Co<sub>x</sub>Fe<sub>2</sub>O<sub>4</sub> ( $0 \leq x \leq 1$  with  $\Delta x = 0.1$ ). The phantoms of each *x* with five different concentrations were placed within a mouse body coil at a time. The mouse body coil was situated isocentrally with the static magnet *B*<sub>0</sub> = 7 T within the homogeneous region. The *B*<sub>1</sub> was the perturbation field with the Larmour frequency 2048 Hz generated by the rf coil.

### *In vivo* magnetic resonance imaging

We procured the *in vivo* *T*<sub>2</sub> weighted FSE MR images using Albino Wister male rats aged 12 to 13 weeks, and body weight 200–250 g. During the *T*<sub>2</sub> W FSE experiment, the rats were made unconscious by administering intramuscular ketamine in a prescribed dose (15 mg kg<sup>-1</sup>).<sup>29</sup> The unconscious rat reclined on a horizontal bed and its head laid inside a head coil generating rf magnetic field *B*<sub>1</sub>. The head coil was isocentric with a static magnetic field (7 T). Throughout the experiment, animals were kept warm with a heater, air supplied at a constant rate, and inspected with a cardiac monitor. At first, *T*<sub>2</sub> W FSE images of the rat brain were acquired without a contrast agent with flip angle (FA) 90°, repetition time (TR) 4000 ms, echo time 45 ms, field of view (FOV) 40  $\times$  40 mm, and image matrix 256  $\times$  256. We inoculated 1 mL chitosan-coated Mg<sub>1-x</sub>Co<sub>x</sub>Fe<sub>2</sub>O<sub>4</sub> nanoparticles of 2 mg mL<sup>-1</sup> concentrated through the tail vein without altering the position. We acquired *T*<sub>2</sub> weighted Fast Spin Echo (FSE) images at intervals of 15, 30, 60, 90, and 120 minutes after inoculating the contrast agents Mg<sub>1-x</sub>Co<sub>x</sub>Fe<sub>2</sub>O<sub>4</sub> ( $0 \leq x \leq 1$  with  $\Delta x = 0.1$ ).

### Animal handling

We handled the animals following The Guide for the Care and Use of Laboratory Animals (1996). We maintained the ARRIVE guidelines for reporting animal research. All necessary efforts were taken to minimize the sufferings of experimental animal



according to the requirement of the Ethical Review Committee of Anima Experiments of Atomic Energy Centre Dhaka, which approved the protocol of with the Memo No: AECD/ROD/EC/21/211.

## Results and discussion

### Structural characterizations

Fig. 1(a and b) presents the X-ray diffraction (XRD) patterns of  $Mg_{1-x}Co_xFe_2O_4$  ( $0 \leq x \leq 1$  with  $\Delta x = 0.1$ ) in the as-dried condition, which were acquired for the structural characterization of all compositions. There was no impurity peak in the XRD spectra within the resolution level of the XRD machine. The samples have a spinel structure<sup>31–33</sup> with the space group of  $Fd\bar{3}m$ . Fig. 1(a) shows that the patterns of Mg-rich compositions up to  $x = 0.4$  consist of broad diffused peaks. The peaks become narrower with the increase in Co. Fig. 1(a and b) shows that while the peaks become sharper, and their positions shifted toward lower values of  $2\theta$ .  $CoFe_2O_4$  has a higher degree of crystallinity than  $MgFe_2O_4$  when NaOH was used as the co-precipitating agent. Absolute lattice parameter was calculated using the Nelson–Riley function. We calculated the lattice parameter for each plane using Bragg's law, and absolute lattice parameters were determined using the Nelson–Riley function,

$$F(\theta) = \frac{1}{2} \left( \frac{\cos^2 \theta}{\sin \theta} + \frac{\cos^2 \theta}{\theta} \right) \quad (3)$$

In Fig. 1(c), the lattice parameter increases with the increase in the cobalt content  $x$  because the ionic radius of the  $Mg^{2+}$  (0.065 nm) ion is smaller than that of the  $Co^{2+}$  (0.072 nm) ion.<sup>34,35</sup> Fig. 1(c) shows that the dependence of the lattice parameter on the composition follows a linear relationship, which follows Vegard's law. Abraham *et al.*<sup>36</sup> synthesized spinel  $Mg_{1-x}Co_xFe_2O_4$  ( $x = 0.0, 0.2, 0.4, 0.6, 0.8$ , and  $1.0$ )

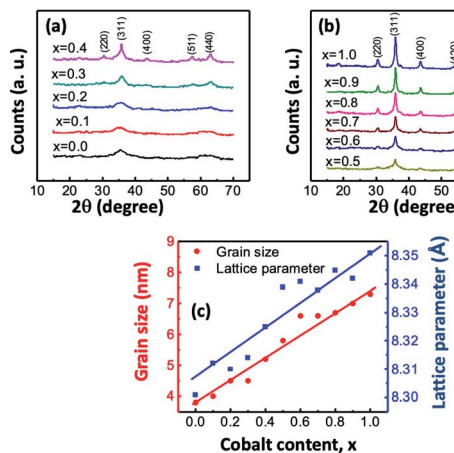


Fig. 1 (a) and (b) XRD traces of  $Mg_{1-x}Co_xFe_2O_4$  ( $0 \leq x \leq 1$  with  $\Delta x = 0.1$ ) in the as-synthesized condition acquired in the range of  $15\text{--}70^\circ$  using  $CuK_\alpha$  radiation with a scan step size of  $0.0167^\circ$ . The peaks are indexed in the figures. (c) Variation of the lattice parameter and grain size with the cobalt content  $x$  in the  $Mg_{1-x}Co_xFe_2O_4$  series.

nanocomposites by modified sol-gel combustion method and found that the lattice parameter increases with an increase in the cobalt content  $x$  and the value of the lattice constant is  $8.303\text{ \AA}$  for  $MgFe_2O_4$ , which is close to the values obtained in the current study. Stein *et al.*<sup>37</sup> synthesized  $CoFe_2O_4$  nanoparticles by chemical coprecipitation method, and its lattice parameter was  $8.358\text{ \AA}$ , which is close to the lattice parameters of  $CoFe_2O_4$  of  $8.351\text{ \AA}$  in this study.

We calculated the grain size of each composition using the Debye–Scherrer's formula:

$$D_P = \frac{0.94\lambda}{\beta \cos \theta} \quad (4)$$

where,  $D_P$  is the average crystallite size,  $\beta$  is the full width at half the maximum of the highest intensity (311) peak,  $\theta$  is the Bragg angle, and  $\lambda$  is the X-ray wavelength. The peak width was estimated using the peak fit option of the X'Pert Highscore Software. Fig. 1(c) presents the variations in the grain size with  $x$ . The grain sizes of  $x = 0$  and  $1$  were  $3.8$  and  $7.3$  nm, respectively. The grain size varies almost linearly with  $x$ . Lodhi *et al.*<sup>32</sup> also obtained that the particle size increases with an increase in the cobalt content,  $x$  of  $Mg_{0.5}Co_xZn_{0.5-x}Fe_2O_4$  prepared by the micro emulsion method.

### Transmission electron microscopy

Fig. 2 shows a representative TEM image of bare and chitosan-coated  $Mg_{0.1}Co_{0.9}Fe_2O_4$  nanoparticles from the  $Mg_{1-x}Co_xFe_2O_4$  series. The magnetic dipole interactions between ferrite

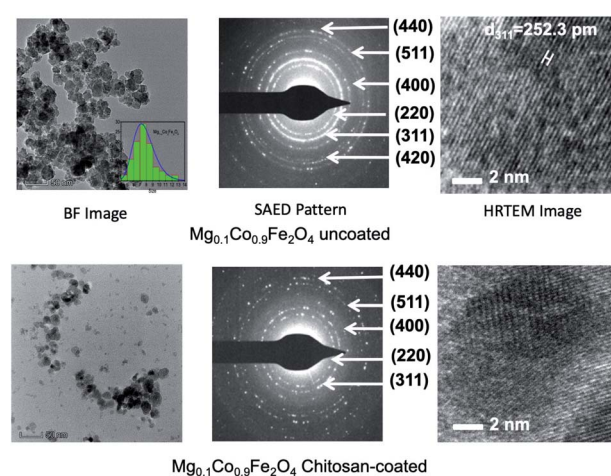


Fig. 2 TEM images of uncoated and chitosan-coated  $Mg_{0.1}Co_{0.9}Fe_2O_4$  nanoparticles. In this figure representative TEM images of the  $Mg_{1-x}Co_xFe_2O_4$  series are presented. In the upper panel, the BF image, SAED pattern, and HRTEM images for the uncoated nanoparticles are presented. In the bottom panel, the BF images, SAED patterns, and HRTEM images of chitosan-coated nanoparticles are presented. We see from the BF images in the figure that the uncoated nanoparticles are aggregated and the coated nanoparticles are dispersed. The SAED patterns show that the lines are more intense for the uncoated samples, as compared to the coated samples since the coated nanoparticles are more dispersed. HRTEM images of the uncoated and coated nanoparticles demonstrate good crystallinity in the as-dried condition.



nanoparticles cause the bare particles to cluster.<sup>36</sup> The dipole interactions are decreased and the particles are dispersed after coating with chitosan. The histogram of the size distribution follows a log-normal distribution (in the inset of the BF image). The average nanoparticle size in the BF image of  $Mg_{0.1}Co_{0.9}Fe_2O_4$  was 7.4 nm, which fits reasonably well with the 7.2 nm reported by XRD. The selected area electron diffraction (SAED) patterns of bare and chitosan-coated  $Mg_{0.1}Co_{0.9}Fe_2O_4$  nanoparticles are shown in Fig. 2. The SAED patterns show that the (311) is the highest intensity plane along with the other planes (220), (400), (420), (511), and (440) indexed in the figure. The *d*-values of the SAED pattern were determined using the Velox software, and the diffractograms were indexed accordingly. The SAED patterns are compatible with the noncrystalline structure reported in the literature.<sup>37–39</sup> The Debye circles are more intense for uncoated than the coated nanoparticles because of the higher degree of dispersion in the coated particles in a region. Fig. 2 also presents the high-resolution transmission electron microscopy (HRTEM) images of bare and chitosan-coated particles. The lattice fringes of the HRTEM image of both bare and chitosan-coated particles in Fig. 2 indicate high crystallinity. The HRTEM image yielded a *d* value of 252 pm, which corresponds to the (311) plane. In Fig. S-1,† the HRTEM images of all  $Mg_{1-x}Co_xFe_2O_4$  ( $0 \leq x \leq 1$  with  $\Delta x = 0.1$ ) compositions in the as-synthesized condition are shown.

The HRTEM images show that all the nanoparticles are crystalline, with the degree of crystallinity increasing as the cobalt concentration *x* increases. Lattice fringes are more prominent in the HRTEM image with higher cobalt content. This is because of the higher degree of crystallinity with the increase of Co. The figure also indicates that the particle size increases with the increase of cobalt in  $Mg_{1-x}Co_xFe_2O_4$  ( $0 \leq x \leq 1$  with  $\Delta x = 0.1$ ) in the as-synthesized conditions.

Fig. 3 displays the STEM image of chitosan-coated  $Mg_{0.1}Co_{0.9}Fe_2O_4$  nanoparticles using the HAADF detector, as well as electron diffraction spectroscopy (EDS) spectra and mapping of the constituent elements Fe, Mg, Co, and O. The mapping of the chitosan constituent atoms, such as carbon (C) and nitrogen (N), is also shown. The STEM-EDS mapping in the figure indicates that the ferrite nanoparticles are chemically homogeneous. The chitosan coating on ferrite nanoparticles is remarkable, as seen by the uniform distribution of C and N atoms. Chitosan is only applied to the nanoparticles as a coating, and the thickness of the coating is very thin. From the STEM EDS mapping, we found the atomic percent of Mg, Co, Fe, and O to be 4.11% ( $\pm 0.86$ ), 8.6%5 ( $\pm 1.31$ ), 12.86% ( $\pm 1.94$ ), and 74.39% ( $\pm 5.36$ ), and the mass percent of Mg, Co, Fe, and O to be 3.96% ( $\pm 0.81$ ), 20.25% ( $\pm 2.87$ ), 28.52 ( $\pm 4.03$ ), and 47.27% ( $\pm 2.31$ ), respectively. From the EDS spectrum of chitosan-coated  $Mg_{0.1}Co_{0.9}Fe_2O_4$  particles, we see the peaks of C (0.28 keV), N (0.39 keV), O (0.53 keV), Fe-L (0.71 keV), Cu-L (0.79 keV), Co-L (0.93 keV), Mg (1.27 keV), Fe-ka (6.42 keV), Co-ka (6.96 keV), Co-kb (7.68 keV), Cu-ka (8.07 keV), and Cu-kb (8.91 keV). Because of the carbon-coated copper grid, the C and Cu peaks in the EDS spectrum have a high intensity. Also, there are no impurity peaks.

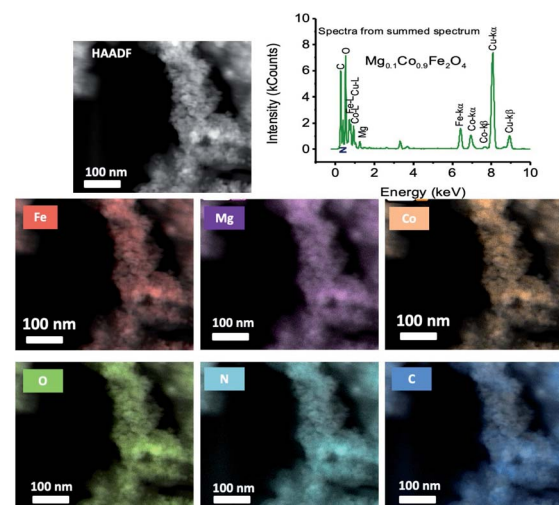


Fig. 3 Scanning transmission electron microscopy (STEM) image of chitosan-coated  $Mg_{0.1}Co_{0.9}Fe_2O_4$  nanoparticles using the HAADF detector, along with the electron diffraction spectroscopy (EDS) mapping of the constituent elements Fe, Mg, Co and O. The mapping of the constituent atoms of chitosan such as carbon (C) and nitrogen (N) atoms are also presented. In the figure, the EDS spectrum of chitosan-coated  $Mg_{0.1}Co_{0.9}Fe_2O_4$  particles is given.

### Mössbauer spectroscopy

Fig. 4 presents the Mössbauer spectra at room temperature of  $Mg_{1-x}Co_xFe_2O_4$  ( $0 \leq x \leq 1$  with  $\Delta x = 0.1$ ) in the dried condition. We used the WMOSS 4R program to analyze the spectrum. Table 1 presents the hyperfine parameters of isomer shift, quadrupole splitting, and hyperfine magnetic field with *x*. We obtained the hyperfine parameters by model fitting the experimental data. The goodness of fit  $\chi^2$  varies between 0.641 to

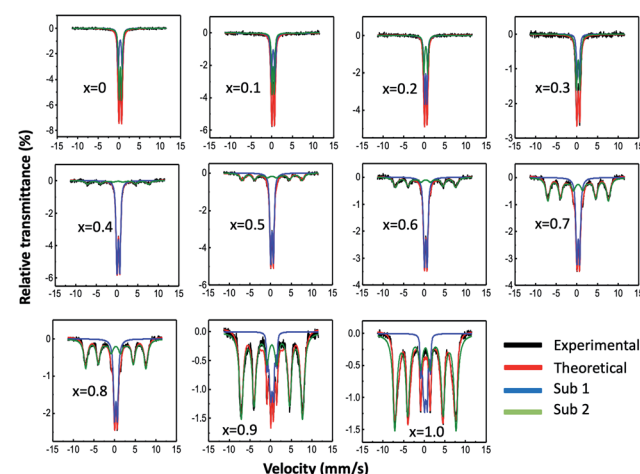


Fig. 4 Mössbauer spectra at room temperature of  $Mg_{1-x}Co_xFe_2O_4$  ( $0 \leq x \leq 1$  with  $\Delta x = 0.1$ ) in the as-dried condition. The spectra were acquired at room temperature without any applied field. In the figure, the black lines represent the experimental data, and the red lines represent the model fitting. The blue and green lines represent the contributions of subspectra 1 and 2, respectively, determined by model fitting using the WMOSS 4R software.



3.112, which is within acceptable limits.<sup>38,39</sup> Manova *et al.*<sup>40</sup> showed that the  $\text{Fe}^{3+}$  sub-spectrum with a larger isomer shift represents octahedral B-sites while the  $\text{Fe}^{3+}$  sub-spectrum with a lower isomer shift represents tetrahedral A-sites. The covalent bond of the A-sites is more potent than that of the B-sites because of the larger internuclear separation of ferric and oxygen ions at the B-site than the A-site, and the orbital overlap is smaller at the B-site than the A-site.<sup>41</sup> However, the site occupancy cannot be determined accurately with zero field measurements for this series of spinel because of the short-range order of the ferric ions surrounded by the nonmagnetic ions. The area of doublets decreases, and that of the sextets increases. Lin *et al.*<sup>39</sup> observed a decrease in the hyperfine field on both the A- and B-sites of  $\text{CoAl}_x\text{Fe}_{2-x}\text{O}_4$  ferrite nanoparticles with an increase in the nonmagnetic  $\text{Al}^{3+}$  content. The spectra with lower cobalt content ( $0 \leq x \leq 0.3$ ) were superparamagnetic with two distinct doublets. In these samples, nonmagnetic  $\text{Mg}^{2+}$  ions surround the  $\text{Fe}^{3+}$  ions, which are magnetically short-range ordered, which lowers the magnetic moment of these samples, and we observed fast relaxation.<sup>39</sup> For spectra with higher cobalt content ( $0.4 \leq x \leq 1.0$ ), model fitting was satisfactory considering one sextet and one doublet subspectra, which shows mixed relaxation. Quadrupole splitting is higher for the doublet subspectra than for the sextets.<sup>42</sup> For cobalt ferrite, the area of the subspectra representing slow relaxation of the ferrimagnetic contribution was the highest. The isomer shifts are in the range of 0.250–0.338, which matches well with the literature.<sup>43</sup> The values of isomer shift reveal that iron exists only in the trivalent state ( $\text{Fe}^{3+}$ ), which belong to the range of 0.1–0.5 and there is no  $\text{Fe}^{2+}$  having isomer shift  $>0.5$ . The fact that the areas of the

subspectra representing the sextet decrease with the decrease in cobalt (Table 1) because of the ferrimagnetic to superparamagnetic transition, which corroborates with the results obtained from the physical property measurement system (PPMS) presented later.<sup>40,41,44–46</sup>

#### Fourier-transform infrared spectroscopy

Fig. 5(a) shows the representative FTIR spectrum of chitosan, bare, and chitosan-coated  $\text{Co}_{0.2}\text{Mg}_{0.8}\text{Fe}_2\text{O}_4$  nanoparticles in the range of  $350$ – $3000\text{ cm}^{-1}$ . A small amount of sample was placed on the diamond/ZnSe crystal of ATR using a pressure arm, which allows good contact of the sample with the crystal. The bare and chitosan samples were in the powder form and the coated samples were in the liquid form. The ESI, Fig. 2 $\dagger$  represents the FTIR spectrum of all compositions of the series  $\text{Mg}_{1-x}\text{Co}_x\text{Fe}_2\text{O}_4$  ( $0 \leq x \leq 1$  with  $\Delta x = 0.1$ ).

We see in Fig. 5(a) and the ESI, Fig. 2 $\dagger$  that the peaks of pure chitosan are at  $890$ ,  $1402$ ,  $1638$ ,  $2896$ , and  $3482\text{ cm}^{-1}$  which are the characteristic absorption bands of chitosan. The absorption peaks at  $3482\text{ cm}^{-1}$  and  $2896\text{ cm}^{-1}$  were present due to the stretching vibration of O-H and -CH<sub>2</sub> pyranose rings, respectively. The presence of absorption peaks at  $1638\text{ cm}^{-1}$  was due to the N-H bending vibration of the amino (-NH<sub>2</sub>) group. An absorption peak at  $1402\text{ cm}^{-1}$  represents the C-H bending vibration of the alkali group. The absorption peaks at  $1058$  and  $890\text{ cm}^{-1}$  represent the antisymmetric stretching vibration of the C-O-C bridges of the glucopyranose ring in the chitosan matrix.<sup>47,48</sup> Two peaks of the bare nanoparticles at the lower frequency region are due to the characteristic absorption bands of the cubic spinel structure.<sup>32–35</sup> A lower frequency absorption

Table 1 Hyperfine parameters derived from the Mössbauer spectroscopy acquired at room temperature and zero-field conditions

<i>x</i>	Position of $\text{Fe}^{3+}$	IS ( $\text{mm s}^{-1}$ )	QS ( $\text{mm s}^{-1}$ )	Hyperfine magnetic field (kG)	Area
0	Doublet	0.327	0.939	—	0.395
	Doublet	0.338	0.555	—	0.597
0.1	Doublet	0.337	0.531	—	0.670
	Doublet	0.338	0.903	—	0.431
0.2	Doublet	0.335	0.506	—	0.473
	Doublet	0.334	0.864	—	0.480
0.3	Doublet	0.323	0.532	—	0.348
	Doublet	0.320	0.871	—	0.596
0.4	Doublet	0.332	0.631	—	0.651
	Sextet	0.327	0.022	449	0.405
0.5	Doublet	0.325	0.663	—	0.862
	Sextet	0.250	0.169	457	0.202
0.6	Doublet	0.329	0.650	—	0.652
	Sextet	0.303	0.060	453	0.430
0.7	Doublet	0.326	0.656	—	0.453
	Sextet	0.300	0.014	456	0.688
0.8	Doublet	0.325	0.669	—	0.418
	Sextet	0.293	0.047	494	0.730
0.9	Doublet	0.276	0.674	—	0.207
	Sextet	0.295	0.270	512	0.895
1.0	Doublet	0.304	0.220	—	0.055
	Sextet	0.299	0.299	518	0.997



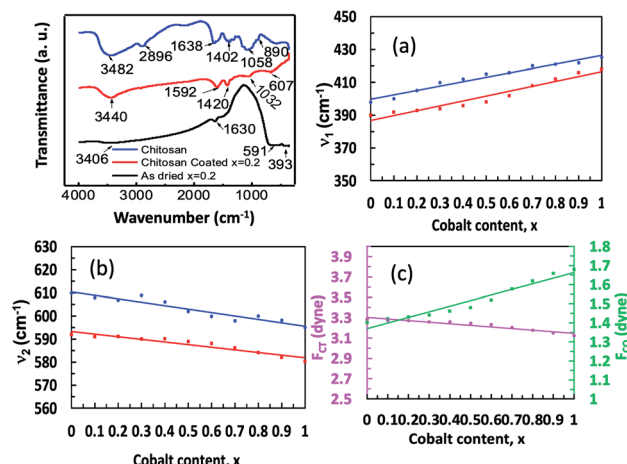


Fig. 5 FTIR spectrum of chitosan, bare nanoparticles and chitosan-coated  $Mg_{1-x}Co_xFe_2O_4$  ( $0 \leq x \leq 1$  with  $\Delta x = 0.1$ ) nanoparticles in the range of  $350$ – $3000$   $cm^{-1}$ . The samples were placed on the diamond/ZnSe crystal of ATR using a pressure arm, which allows good contact between the sample and the crystal. The bare and chitosan samples were in the powder form and the coated samples were in the liquid form. (a) A representative FTIR spectrum of chitosan, bare and chitosan-coated  $Co_{0.2}Mg_{0.8}Fe_2O_4$  nanoparticles in the range of  $350$ – $3000$   $cm^{-1}$ . (b) Variations of lower frequency absorption band ( $\nu_1$ ), (c) higher frequency absorption band ( $\nu_2$ ) of the bare (red) and coated (blue) nanoparticles. (d) Variations of force constants  $F_{CT}$  (magenta) and  $F_{CO}$  (green) of tetrahedral and octahedral sites, respectively, with  $x$ .

band ( $\nu_1$ ) is observed in the range of  $390$  to  $418$   $cm^{-1}$ , and a higher frequency absorption band ( $\nu_2$ ) is observed in the range of  $580$  to  $592$   $cm^{-1}$ . The lower frequency band ( $\nu_1$ ) represents the stretching vibration of the metal-oxide bond at the octahedral site, while the higher frequency band ( $\nu_2$ ) represents the stretching vibration of the metal-oxide bond at the tetrahedral site.

Fig. 5(b) and (c) show the variations of  $\nu_1$  and  $\nu_2$  of bare and coated nanoparticles with the cobalt content  $x$ . It is interesting to note that the variations of  $\nu_1$  and  $\nu_2$  with  $x$  are linear for both bare and coated nanoparticles. The standard mode of vibration of the tetrahedral site ( $\nu_2$ ) is higher than that at the octahedral site ( $\nu_1$ ) because of the shorter bond length of the tetrahedral site than the octahedral site.<sup>35,36</sup> With the increase in  $x$ , the occupation of  $Co^{2+}$  ions at the octahedral sites increases, thus reducing the bond length at this site. The preference of  $Mg^{2+}$  ions is for the tetrahedral sites. Therefore, with the increase in  $x$ , the bond length at the octahedral sites reduces with a corresponding increase in the bond length at the tetrahedral sites for which  $\nu_1$  increases and  $\nu_2$  decreases with cobalt content  $x$ . For the coated  $Mg_{1-x}Co_xFe_2O_4$  nanoparticles, however, the  $\nu_1$  and  $\nu_2$  show a shift of the absorption band toward the higher wave number compared to the as-dried nanoparticles due to the bonding of ferrite with chitosan.<sup>49</sup> The force constant tells us the stiffness of the  $Fe^{3+}$  ions to the vibrational displacement considering other nuclei at their equilibrium position. Force constants are inversely related to the bond length of  $Fe^{3+}$  and the nearest neighbor ions. We obtained the force constants (FC)

for the tetrahedral A site ( $F_{CT}$ ) and the octahedral B site ( $F_{CO}$ ) by the following relation.

$$F_c = 4\pi^2 C^2 \nu^2 m \quad (5)$$

In the above equation,  $c$  is the speed of light  $\sim 2.99 \times 10^{10}$   $cm s^{-1}$ ,  $\nu$  is the vibrational frequency of the ions at the A- and B-sites,  $m$  is the reduced mass for the  $Fe^{2+}$  and  $O^{2-}$  ions, which is  $2.061 \times 10^{-23}$  g. Fig. 5(d) shows that the value of  $F_{CT}$  is lower than  $F_{CO}$  because of the higher orbital overlap at the tetrahedral site. However,  $F_{CT}$  decreases and  $F_{CO}$  increases with increasing cobalt content  $x$ , which indicates that the orbital overlap at the A-site decreases and that at the B-site increases with  $x$ , i.e., Co concentration<sup>46</sup> because of the preference of Co at the B-site.

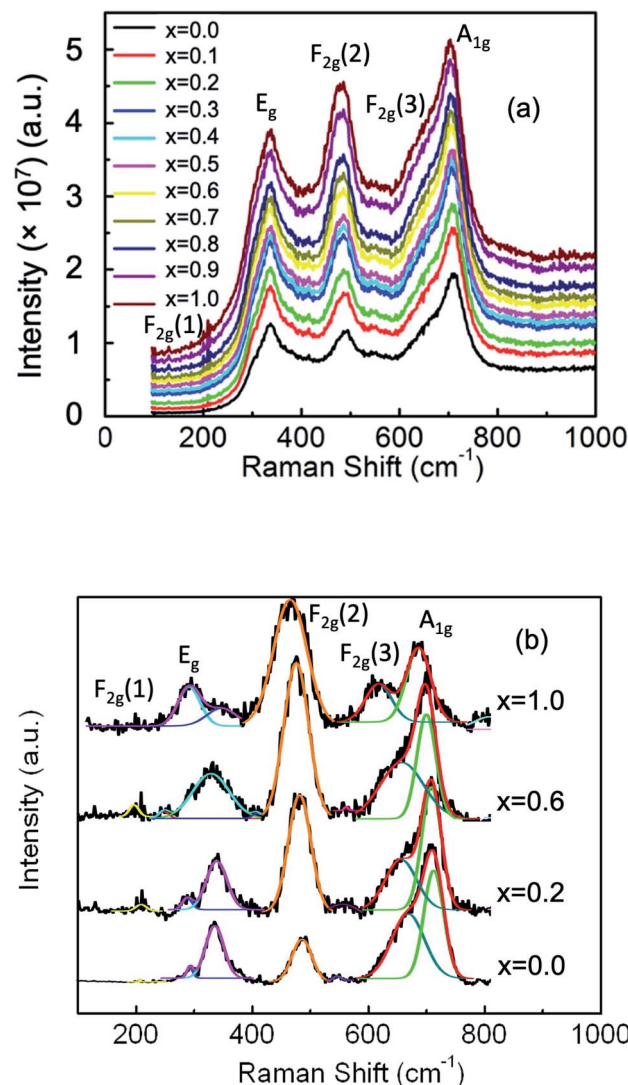


Fig. 6 (a) Room temperature Raman spectra of  $Mg_{1-x}Co_xFe_2O_4$  ( $0 \leq x \leq 1$  with  $\Delta x = 0.1$ ) nanoparticles in the range of  $190$ – $1000$   $cm^{-1}$  using the pelletized solid samples. Five Raman active modes  $A_{1g}$ ,  $E_g$ ,  $F_{2g}(1)$ ,  $F_{2g}(2)$ , and  $F_{2g}(3)$  are assigned in the Raman spectra. (b) Representative best fitting of the Raman spectra using the Gaussian function after background subtraction and deconvolution.



**Table 2** Wavenumbers of the five Raman active modes  $A_{1g}$ ,  $E_g$ ,  $F_{2g}(1)$ ,  $F_{2g}(2)$ , and  $F_{2g}(3)$  of  $Mg_{1-x}Co_xFe_2O_4$  ( $0 \leq x \leq 1$  with  $\Delta x = 0.1$ ) assigned to the Raman spectra

x	Main Raman mode peak energy ( $\text{cm}^{-1}$ )					
	$F_{2g}(1)$	$E_g$	$F_{2g}(2)$	$F_{2g}(3)$	$A_{1g}$ Me-O	$A_{1g}$ Fe-O
0.0	211	292	487	549	667	712
0.1	205	333	480	548	667	707
0.2	208	335	478	553	668	706
0.3	214	338	478	557	658	704
0.4	211	345	479	620	652	701
0.5	223	330	474	555	661	697
0.6	200	329	474	555	660	697
0.7	—	292	478	566	655	695
0.8	—	294	478	577	653	696
0.9	—	320	471	—	619	691
1.0	—	300	472	—	619	690

## Raman spectroscopy

We used Raman spectroscopy to further investigate the structure of the nanoparticles by identifying several vibrational modes.<sup>50–53</sup> Fig. 6(a) shows the Raman spectra of  $Mg_{1-x}Co_xFe_2O_4$  ( $0 \leq x \leq 1$  with  $\Delta x = 0.1$ ) nanoparticles in the range of 190–1000  $\text{cm}^{-1}$  at ambient temperature. We saw earlier that  $Mg_{1-x}Co_xFe_2O_4$  ferrites have a partially inverse spinel structure, which is associated with the space group ( $Fd\bar{3}m$ ).<sup>51,54–57</sup> The vibrational modes associated with this space group are  $A_{1g}$  (R),  $E_g$  (R),  $F_{1g}$ ,  $3F_{2g}$  (R),  $2A_{2u}$ ,  $2E_u$ ,  $4F_{1u}$  (IR), and  $2F_{2u}$ . Notation R implies Raman active vibrational modes, IR symbolizes infrared-active vibrational modes, and the rest are silent modes. Therefore, five Raman active modes  $A_{1g}$ ,  $E_g$ ,  $F_{2g}(3)$ ,  $F_{2g}(2)$ , and  $F_{2g}(1)$  are expected to be observed in the Raman spectra. Fig. 6(b) presents the discernible Raman modes of the studied

samples. The  $A_{1g}$  modes are associated with symmetric stretching of  $\text{MeO}_4$  (Me represents Co and/or Mg) and stretching of  $\text{FeO}_4$  at the A-site. The  $E_g$  modes represent bending of oxygen with respect to Fe at the B-site. The  $F_{2g}(3)$  modes represent the antisymmetric bending of oxygen with respect to Fe, the  $F_{2g}(2)$  modes represent the asymmetric stretching of Fe and O, and the  $F_{2g}(1)$  modes represent the complete translational motion of Fe and O.<sup>55,58</sup> The Raman peaks in the region of 660–720  $\text{cm}^{-1}$  represent the vibrational modes of the A-site, and the Raman peaks in the region of 460–660  $\text{cm}^{-1}$  represent the vibrational modes of the B-site of the ferrites. Table 2 presents the wavenumbers of five Raman active modes  $A_{1g}$ ,  $E_g$ ,  $F_{2g}(1)$ ,  $F_{2g}(2)$ , and  $F_{2g}(3)$  of  $Mg_{1-x}Co_xFe_2O_4$  ( $0 \leq x \leq 1$  with  $\Delta x = 0.1$ ) assigned to the Raman spectra. The wavenumber of the  $A_{1g}$  vibrational modes lowers with an increase in the cobalt content  $x$  because the atomic mass of Co (58.9332 amu) ions is higher than that of Mg (24.3050 amu) ions. Mund *et al.*<sup>52</sup> also found an increase in the vibrational mode (blue shift) when Mg is increased in magnesium cobalt ferrite prepared by the sol-gel auto-combustion method because of the lower atomic mass of Mg than Co.

Fig. 7 presents the variations in the area integrals with the cobalt concentration  $x$ , which were obtained by the Gaussian fitting of  $A_{1g}$ ,  $E_g$ ,  $F_{2g}(3)$ ,  $F_{2g}(2)$ , and  $F_{2g}(1)$  peaks assigned to the Raman spectra. After background subtractions and deconvolution, the Gaussian function produced the best fit between the experimental and theoretical data. Fig. 7 shows that for  $x = 0$ , the area integral for  $A_{1g}$ , *i.e.*, the peaks representing tetrahedral sites for both Me-O and Fe-O, is the highest, indicating that the cation occupancy at the A-site is the highest (where Me represents Mg and Co and Fe for iron). The area integral of  $A_{1g}$  of both Me-O and Fe-O is depicted in Fig. 7, which shows that

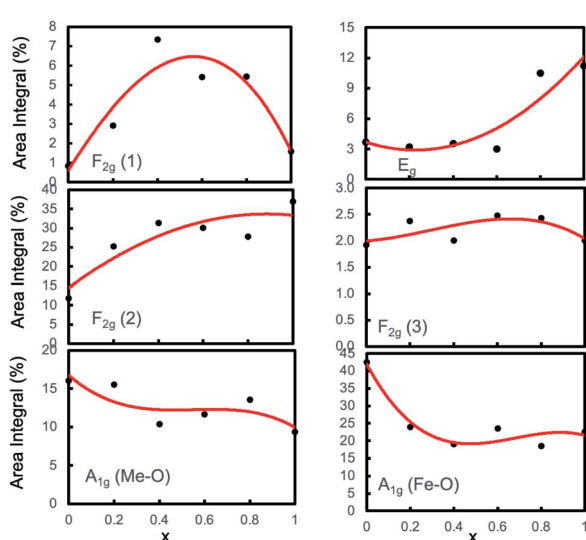


**Fig. 7** Variation of area integral with Co concentration  $x$  of the  $A_{1g}$ ,  $E_g$ ,  $F_{2g}(1)$ ,  $F_{2g}(2)$ , and  $F_{2g}(3)$  peaks assigned to the Raman spectra of the  $Mg_{1-x}Co_xFe_2O_4$  nanoparticles obtained by Gaussian fitting and deconvolution.

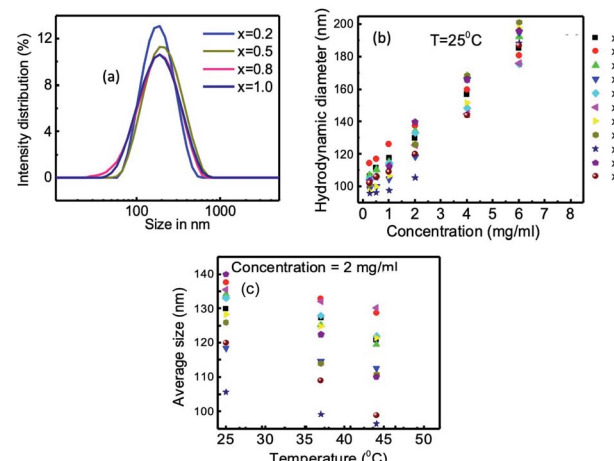


**Fig. 8** Hydrodynamic size distribution of chitosan-coated  $Mg_{1-x}Co_xFe_2O_4$  ( $0 \leq x \leq 1$  with  $\Delta x = 0.1$ ) nanoparticles measured at 25 °C for the concentrations of 2 and 4 mg  $\text{mL}^{-1}$ . (a) Representative intensity distribution of hydrodynamic sizes of  $x = 0.2$ ,  $0.5$ ,  $0.8$ , and  $1.0$ . (b) Variation of hydrodynamic size with concentration of the solution of chitosan-coated  $Mg_{1-x}Co_xFe_2O_4$  nanoparticles. (c) Variation of average hydrodynamic size with temperature at the concentration of 2 mg  $\text{mL}^{-1}$  chitosan-coated  $Mg_{1-x}Co_xFe_2O_4$  nanoparticles.



when  $x$  increases, the occupancy of Me and Fe ions decreases. The integral area of  $E_g$ ,  $F_{2g}(2)$  and  $F_{2g}(3)$ , on the other hand, increases with  $x$ , indicating that the occupancy of Me and Fe at the B-site increases with  $x$ , resulting in a higher degree of inverse spinel structure. We know that cobalt prefers to occupy the B-sites, while Mg prefers to occupy the A-sites. As the cobalt concentration  $x$  increases, the area integral of the peaks of  $A_{1g}$  decreases, resulting in a rise of the lower modes, namely,  $E_g$  and  $F_{2g}$ .

### Hydrodynamic diameter and zeta potential

We measured the hydrodynamic size distribution of chitosan-coated  $Mg_{1-x}Co_xFe_2O_4$  ( $0 \leq x \leq 1$  with  $\Delta x = 0.1$ ) nanoparticles at  $25^\circ C$  temperature for the concentration of 2 and  $4 \text{ mg mL}^{-1}$ . Fig. 8(a) and S-3† show some representative data of the intensity distribution of the hydrodynamic sizes for  $x = 0.2$ , 0.5, 0.8, and 1.0. Dynamic light scattering (DLS) measures Brownian motion, which is the random movement of particles due to the interactions with the solvent molecules surrounding them, correlating to the particle size in the solution.<sup>59</sup> It is noticeable from Fig. 8(a) that the curves are symmetric. The hydrodynamic size of the particles from the translational diffusion coefficient uses the Stokes-Einstein equation<sup>59</sup>

$$d(H) = \frac{kT}{3\pi\eta D} \quad (6)$$

where  $d(H)$  is the hydrodynamic diameter,  $D$  is the translational diffusion coefficient,  $k$  is the Boltzmann's constant,  $T$  is the absolute temperature, and  $\eta$  is the viscosity of the solution. The hydrodynamic diameters of bare nanoparticles at  $2 \text{ mg mL}^{-1}$  were in the range from 2000 to 8000 nm. In the as-dried condition, agglomeration causes the formation of large

particles in water, which results in sedimentation.<sup>59</sup> The TEM images presented in Fig. 2 confirmed the agglomeration of the uncoated samples, whereas the chitosan-coated particles are highly dispersed. Fig. 8(b) presents the concentration dependence of the hydrodynamic diameters of the chitosan-coated nanoparticles of  $Mg_{1-x}Co_xFe_2O_4$  for different values of  $x$ . The hydrodynamic diameters of the nanoparticles in Fig. 8(b) increase with an increase in the concentration of the solution in water. Fig. 8(c) and S-3† present the temperature dependence of hydrodynamic diameters of coated nanoparticles for 2 and  $4 \text{ mg mL}^{-1}$ , respectively. The hydrodynamic diameter decreases with an increase in the temperature for both the concentrations. The corresponding polydispersity indexes were in the range from 0.11 to 0.29 only, which are suitable for biomedical applications.

Fig. 9 and S-4† present the variation in the zeta potential of chitosan-coated  $Mg_{1-x}Co_xFe_2O_4$  ( $0 \leq x \leq 1$  with  $\Delta x = 0.1$ ) nanoparticles with the pH of the solution. The zeta potential of the chitosan-coated  $Mg_{1-x}Co_xFe_2O_4$  nanoparticles was greater than 30 mV at pH 2.5 to 5, which means that the nanoparticles are stable in this region. The isoelectric zeta potentials of the solution were from pH 9 to 10.5. The un-coated  $Mg_{1-x}Co_xFe_2O_4$  particles with concentration  $4 \text{ mg mL}^{-1}$ , which were from -2 mV to 6.45 mV, and their pH was in the range from 6.25 to 6.70, which also means that the particles are unstable in water. In Fig. 9, the zeta potential of the chitosan-coated  $Mg_{1-x}Co_xFe_2O_4$  particles of concentration  $4 \text{ mg mL}^{-1}$  was in the range from 30 to 50 mV, and their pH was from 3.45 to 4.55. Zahraei *et al.*<sup>60</sup> found the highest value of the zeta potential of chitosan-coated manganese zinc ferrite at pH 3. Arakha *et al.*<sup>61</sup> measured the zeta potential of chitosan-coated iron oxide nanoparticles, resulting in a stable suspension, and that value is 36.3 mV. The zeta potentials of the coated particles of our samples were

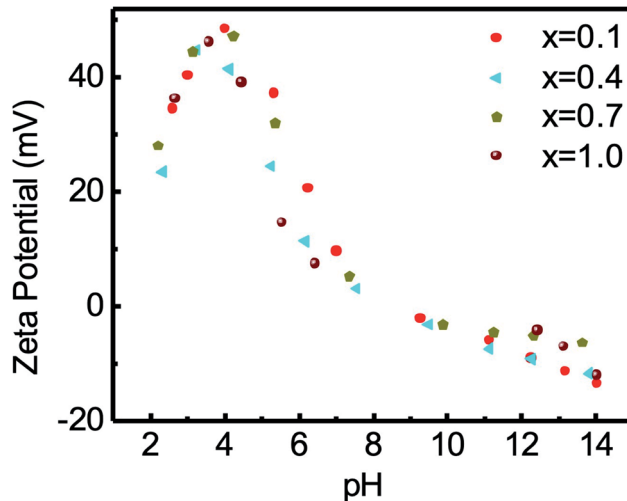


Fig. 9 The variation of zeta potential of chitosan-coated samples with the pH of the solution. The zeta potential of the chitosan-coated  $Mg_{1-x}Co_xFe_2O_4$  ( $0 \leq x \leq 1$  with  $\Delta x = 0.1$ ) particles was greater than 30 at pH 2.5 to 5, which means that the particles are stable in that region. The isoelectric zeta potentials of the solution were at pH 9 to 10.5. In this figure, the representative data for  $x = 0.1$ , 0.4, 0.7, and 1.0 are shown.

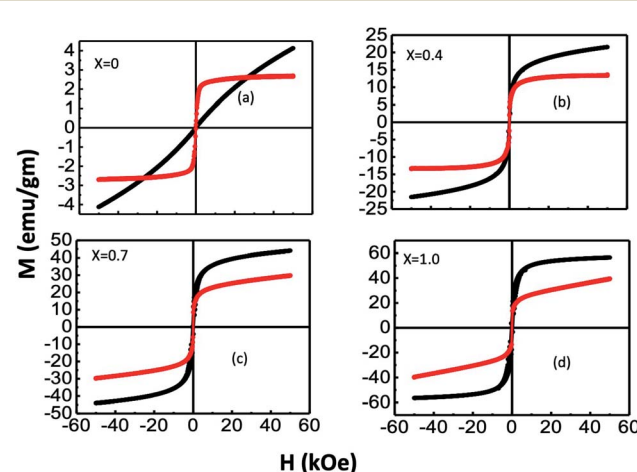


Fig. 10 Representative  $M$ - $H$  curves of (a)  $x = 0$ , (b)  $x = 0.4$ , (c)  $x = 0.7$ , and (d)  $x = 1.0$ . The  $M$ - $H$  loops for bare and chitosan-coated  $Mg_{1-x}Co_xFe_2O_4$  ( $0 \leq x \leq 1$  with  $\Delta x = 0.1$ ) nanoparticles were measured on the powder samples in the bare and liquid samples in coated nanoparticles with a maximum magnetic field of 5 T. Extensive variation in the  $M$ - $H$  curves of bare and coated samples demonstrates that the nanoparticles of all compositions have undergone surface functionalization.



higher than 30 mV, which means that in this pH region, the solution is stable. Even after one year, no precipitation or agglomeration was noticeable in the vial of the solution, indicating that the samples were well coated and dispersed. Therefore, the electrostatic stability occurs in the region of pH 2.5 to 5.5. The isoelectric zeta potentials of the samples were in the pH range from 7 to 8.5. Zahraei *et al.*<sup>60</sup> found that the isoelectric point of chitosan-coated manganese zinc ferrite is 8.5, which is supported by our data. For a higher pH, the zeta potential decreases slowly, and particles may settle down due to flocculation, aggregation, and coagulation. Zeta potential is related to the electrophoretic mobility by Henry equation,<sup>62</sup> which is,

$$U_E = \frac{2\epsilon_r \epsilon_0 \zeta F(\kappa a)}{3\eta} \quad (7)$$

where  $U_E$  is electrophoretic mobility,  $\epsilon_r$  dielectric constant,  $\epsilon_0$  is the permittivity of vacuum,  $\zeta$  is zeta potential,  $F(\kappa a)$  is Henry's function, and  $\eta$  is the viscosity of the solution at the experimental temperature. Thus, zeta potential depends on the concentration of the particles, the viscosity, and the pH of the solution.

### Magnetic measurements

We measured the variations in the magnetization ( $M$ ) with an applied field ( $H$ ) for bare and chitosan-coated  $Mg_{1-x}Co_xFe_2O_4$  ( $0 \leq x \leq 1$  with  $\Delta x = 0.1$ ) nanoparticles with a maximum magnetic field of 5 Tesla. Fig. 10 presents the representative  $M$ - $H$  curves of  $x = 0, 0.4, 0.7$ , and  $1.0$ , and Fig. S-5<sup>†</sup> presents the  $M$ - $H$  curves for other values of  $x$ . It is interesting to note that a large difference in the shape of the  $M$ - $H$  curves occurred with composition and chitosan-coating. The surface functionalization of the coated samples causes changes in the shape of  $M$ -

the  $H$  curves of bare and coated samples. For instance, pure  $MgFe_2O_4$ , *i.e.*,  $x = 0$ , bare nanoparticles are superparamagnetic. With the increase  $x$ , there is a transition from superparamagnetic to a mixed superparamagnetic/ferrimagnetic relaxation as evidenced further by the Mössbauer spectroscopy in Fig. 4. Wide variations in the shape of the hysteresis loop between bare and coated particles for  $x = 0$  might be due to the clustering effect in the coated in particles that facilitate exchange interaction and thereby causes ferrimagnetic relaxations with a negligible coercivity and remanence.<sup>63</sup> Because of the enormous surface-to-volume ratio, the magnetic properties of nanoparticles are greatly influenced by their surface atoms. A-B coupling *via* superexchange interaction mediated by oxygen is disrupted at the surface due to insufficient atom coordination. As a result, surface anisotropy is induced by the distribution of the exchange field and crystal field perturbations.<sup>40</sup> The stress anisotropy at the nanoparticles' surface is reduced by chitosan coating, which reduces the total effective anisotropy. As a result, coated particles respond to applied fields faster than bare particles, despite the fact that bare particles have higher magnetization than coated particles. Magnetocrystalline anisotropy increases as  $x$  increases, raising the effective anisotropy,<sup>40</sup> and thereby, magnetic hardness increases with  $x$ .

Using the law of approach to saturation, we estimated the saturation magnetization  $M_s$  for each composition.<sup>64</sup> Fig. 10(a) presents the variation of  $M_s$  with  $x$  for bare and chitosan-coated  $Mg_{1-x}Co_xFe_2O_4$  ( $0 \leq x \leq 1$  with  $\Delta x = 0.1$ ) nanoparticles.  $M_s$  increases with  $x$  because of the higher magnetic moment of cobalt ( $3.88 \mu B$ ) than magnesium ( $0 \mu B$ ).<sup>18,65</sup> The  $M_s$  of the as-dried  $Mg_{1-x}Co_xFe_2O_4$  ( $0 \leq x \leq 1$  with  $\Delta x = 0.1$ ) nanoparticles are  $6.9, 11.4, 14.67, 22.26, 25.21, 32.29, 43.44, 49.12, 55.54, 56.54$ , and  $59.29$  emu g<sup>-1</sup>, respectively. Fig. 11(b-d) shows an increase in the coercive field, remanent magnetization, and anisotropy constant with cobalt supported by Mund *et al.*<sup>18</sup>.

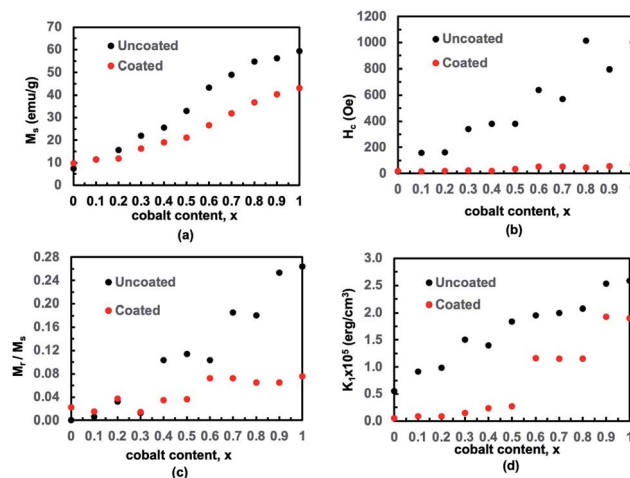


Fig. 11 We determined the saturation magnetization for each composition using the law of approach to saturation. (a) The variation of saturation magnetization with  $x$  for bare and chitosan-coated  $Mg_{1-x}Co_xFe_2O_4$  ( $0 \leq x \leq 1$  with  $\Delta x = 0.1$ ) nanoparticles. The variations in (b) coercive field, (c) remanent magnetization, and (d) anisotropy constant with  $x$ .

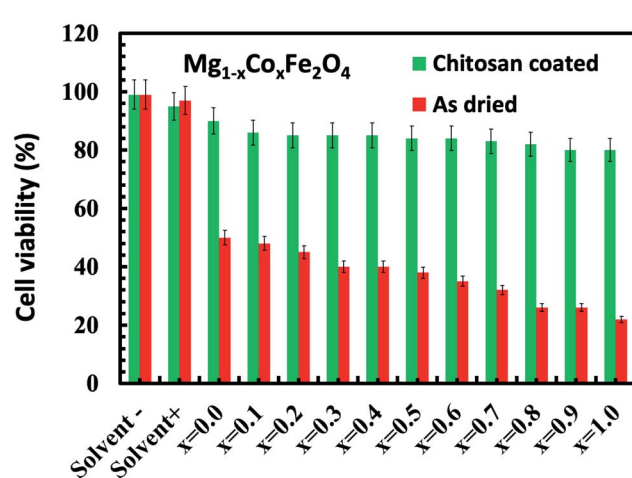


Fig. 12 Cytotoxicity assay of HeLa cells incubated for 48 hours in the DMEM media with the as-dried and chitosan coated as-dried  $Mg_{1-x}Co_xFe_2O_4$  ( $0 \leq x \leq 1$  with  $\Delta x = 0.1$ ) sample. The figure shows that the uncoated  $Mg_{1-x}Co_xFe_2O_4$  nanoparticles in the bare conditions are not viable, while we see a remarkable difference for the chitosan-coated  $Mg_{1-x}Co_xFe_2O_4$  nanoparticles, which are fully viable.



When the  $Mg^{2+}$  is higher, *i.e.*, at lower  $x$ , the magnetic moment is diluted. With the increase in  $x$ , the magnetic moment increases and the magnetocrystalline anisotropy of  $Co^{2+}$  raises the effective anisotropy. Thus, we see an increase in the coercivity and remanent ratio in the bare state. Pervaiz *et al.*<sup>66</sup> synthesized  $CoFe_2O_4$  by sol-gel auto combustion technique. They found the saturation magnetic moment and anisotropy constant to be  $63 \text{ emu g}^{-1}$  and  $0.35 \times 10^6 \text{ erg cm}^{-3}$ , respectively, which are close to the values we reported in the current study.

Fig. 11(a) shows that the magnetization of coated particles is lower than that of the uncoated particles. This is because of the chitosan coating, which is a magnetically dead layer on the surface of the nanoparticles, which inhibits inter-particle exchange interactions of magnetic moments. The chitosan coating also lessens the surface anisotropy and effective anisotropy. Therefore, the values of coercivity and remanent magnetization of the coated particles are lower than that of the uncoated particles.<sup>67-69</sup> The cubic anisotropy constant,  $K_1$ , was determined by the relation<sup>70</sup>

$$M = M_s \left[ 1 - \frac{8}{105} \left( \frac{K_1}{M_s H} \right)^2 \right] + \chi H \quad (8)$$

where  $K_1$  is the cubic anisotropy constant,  $M_s$  is the saturation magnetization by the law of approach to saturation, which characterizes the dependence of magnetization  $M$  on the applied magnetic field for  $H \gg H_c$ , and  $\chi$  is the high-field susceptibility. The cubic anisotropy constant  $K_1$  increases with  $x$  but decreases with the coating. At lower  $x$ , the surface anisotropy effect contributes to the cubic anisotropy. At higher  $x$ , both surface and magnetocrystalline anisotropy contribute to the cubic anisotropy. The coating reduces the surface and stress anisotropy but is unable to lessen the magnetocrystalline

anisotropy. Therefore, in the complete range of chitosan-coated  $Mg_{1-x}Co_xFe_2O_4$ , cubic anisotropy decreases with the coating but increases with  $x$ , *i.e.*, the cobalt content.

### Cytotoxicity

We studied the cytotoxic effect of bare and chitosan-coated  $Mg_{1-x}Co_xFe_2O_4$  ( $0 \leq x \leq 1$  with  $\Delta x = 0.1$ ) nanoparticles using the HeLa cell line. We studied the toxicity effect on the HeLa cell line for the future *in vivo* MRI and hyperthermia studies by inoculating the tumor using HeLa cell lines. For *in vivo* tumor studies, we need to exclude any cytotoxic effect of the nanoparticles on the HeLa cell line. Fig. 12 shows that the uncoated  $Mg_{1-x}Co_xFe_2O_4$  nanoparticles in the bare conditions are not viable. While we see a remarkable difference for chitosan-coated  $Mg_{1-x}Co_xFe_2O_4$  nanoparticles, both chitosan and chitosan-coated  $Mg_{1-x}Co_xFe_2O_4$  nanoparticles were biocompatible because their cell viability was more than 80%. For the as-synthesized  $Mg_{1-x}Co_xFe_2O_4$ , the toxicity increases with an increase in the cobalt content  $x$  for the entire range of composition. The cell viability slightly decreases with an increase in the cobalt content  $x$ .<sup>71-73</sup>

### Hyperthermia

Fig. 13(a) presents the heating profiles of chitosan-coated  $Mg_{1-x}Co_xFe_2O_4$  ( $0 \leq x \leq 1$  with  $\Delta x = 0.1$ ), which shows the rise in the temperature with time for different values of  $x$  and reaches a plateau temperature. The temperature rises with time because of the Néel and Brownian relaxations and hysteresis loss. The Néel relaxation time is,

$$\tau_N = \tau_0 e^{\frac{KV}{k_B T}} \quad (9)$$

where  $K$  is the anisotropy constant, and  $V$  is the volume of the magnetic particles,  $k_B$  is the Boltzmann constant, and  $T$  is the temperature. In Fig. 13(a), the plateau temperature rises with  $Co$  because of the increase in the anisotropy constant and particle size, which generates more heat through Néel's relaxation.

Brownian relaxation is associated with the particle size and viscosity of the solutions of nanoparticles. Brownian relaxation also contributes to the rise in the temperature with time in Fig. 13(a). An increase in the concentration of the colloidal suspension increases the viscosity. With the increase in the  $Co$  content, the size of the nanoparticles increases. Therefore, Brownian relaxation also contributes to the rise in the plateau temperature with  $x$  and magnetic nanoparticles' concentration.<sup>22,74,75</sup> The Brownian relaxation time is,

$$\tau_N = \frac{3\eta V_H}{k_B T} \quad (10)$$

where  $\eta$  is the dynamic viscosity of the carrier liquid,  $V_H$  is the hydrodynamic volume of the particles,  $k_B$  is the Boltzmann constant, and  $T$  is the temperature. The effective relaxation time is

$$\frac{1}{\tau} = \frac{1}{\tau_N} + \frac{1}{\tau_B} \quad (11)$$

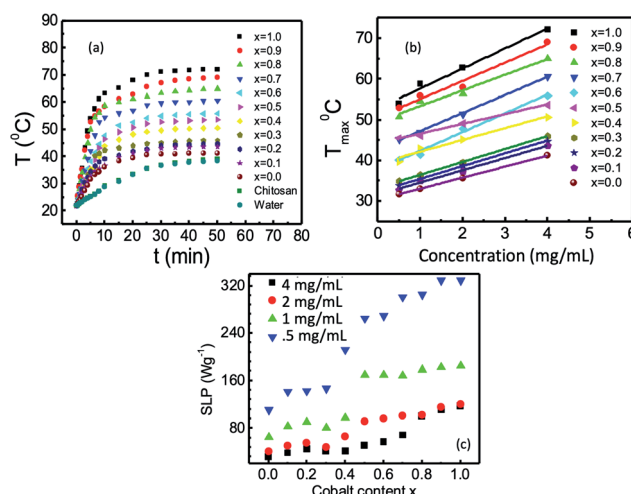


Fig. 13 (a) Rise of temperature as a function of time of chitosan-coated  $Mg_{1-x}Co_xFe_2O_4$  ( $0 \leq x \leq 1$  with  $\Delta x = 0.1$ ) with  $4 \text{ mg mL}^{-1}$  concentration in a rf field of  $26 \text{ mT}$ ; (b) variation of maximum temperature with the concentration of the coated nanoparticles for different values of  $x$ , and (c) variation of specific loss power (SLP) with cobalt content  $x$  of chitosan-coated nanoparticles at concentrations of  $0.5, 1, 2$ , and  $4 \text{ mg mL}^{-1}$ .



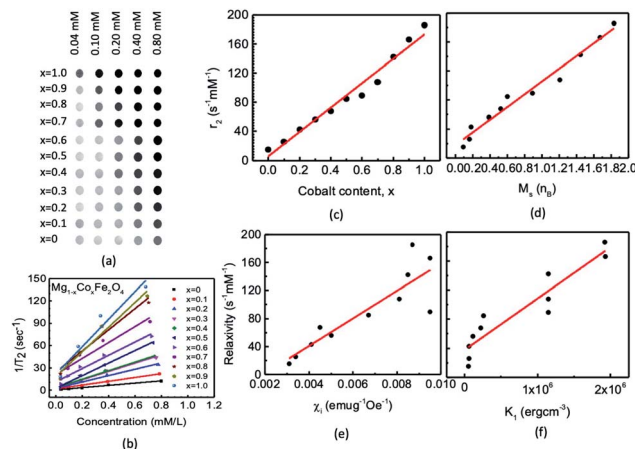


Fig. 14 We acquired phantom images for the chitosan-coated  $Mg_{1-x}Co_xFe_2O_4$  ( $0 \leq x \leq 1$  with  $\Delta x = 0.1$ ) nanoparticles. The  $T_2$  weighted fast spin-echo (FSE) magnetic resonance images were acquired using the machine of model Bo = 7 T; the repetition time (TR) was 4000 ms and the slice thickness (THK) was 1.0 mm, and the FOV was  $40 \times 40$ . We acquired the  $T_2$  mapping at different echo times (TE) of 7 ms, 14 ms, 21 ms, 28 ms, 35 ms, 42 ms, 49 ms, 56 ms, 63 ms, 70 ms, 77 ms, 84 ms, 91 ms, 98 ms, 105 ms, and 112 ms. (a) Slices of different cobalt content  $x$  with concentrations of 0.04, 0.10, 0.20, 0.40, and 0.80 mM in each phantom. (b) Concentration dependence of relaxation with linear fitting, the slope of which provides the values of relaxivity for different values of  $x$ ; (c) variation of relaxivity with cobalt content  $x$ , (d) with saturation magnetization, (e) with susceptibility, and (f) with magnetocrystalline anisotropy.

Fig. 13(b) shows an increase in the maximum temperature (at plateau region)  $T_{\max}$  with the solution concentration for  $0 \leq x \leq 1$  with  $\Delta x = 0.1$ . For the applied field of 26 mT and concentration of  $4 \text{ mg mL}^{-1}$ , the maximum temperature varies between 41 to 72 °C. Fig. 13(b) also demonstrates that for the AC magnetic field of 26 mT, the concentration needed to reach the hyperthermia temperature (42–46 °C) is  $8 \text{ mg mL}^{-1}$  for chitosan-coated  $MgFe_2O_4$ . With the increase in the Co content, *i.e.*, for  $x = 0.1, 0.2$ , and  $0.3$ , the concentration of  $4 \text{ mg mL}^{-1}$ , for  $x = 0.4$  and  $0.5$ , a concentration  $1 \text{ mg mL}^{-1}$ , for  $x = 0.6$  and  $0.7$ , a concentration of  $0.5 \text{ mg mL}^{-1}$ , and for  $x = 0.8, 0.9$ , and  $1$ , a concentration of  $0.25 \text{ mg mL}^{-1}$  are needed. Fig. 13(c) presents the variations in the specific loss power (SLP) at different compositions and concentrations. The SLP increases with an increase in the cobalt content  $x$  and decreases with the increase in the nanoparticles' concentration.<sup>22,74,75</sup>  $MgFe_2O_4$  does not show hyperthermia properties up to  $4 \text{ mg mL}^{-1}$  concentration. However, the minimal substitution of magnesium with cobalt makes the studied samples suitable for hyperthermia at  $4 \text{ mg mL}^{-1}$  concentration.

### Magnetic resonance imaging (MRI)

We acquired the  $T_2$  map of phantoms containing chitosan-coated  $Mg_{1-x}Co_xFe_2O_4$  ( $0 \leq x \leq 1$  with  $\Delta x = 0.1$ ) nanoparticles with different concentrations. The parameters for the imaging were 7 Tesla static magnetic field with a flip angle (FA) of 90°, repetition time (TR) of 4000 ms, and echo times (TE) were 7 ms, 14 ms, 21 ms, 28 ms, 35 ms, 42 ms, 49 ms, 56 ms, 63

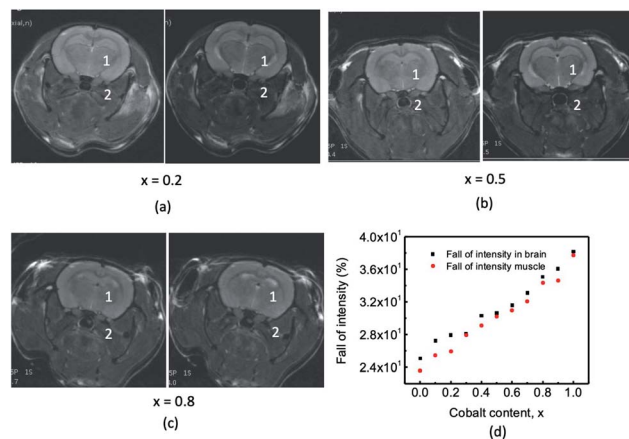


Fig. 15 The  $T_2$  weighted MRI imaging of rat brain using the Fast Spin Echo (FSE) pulse sequence. Some representative  $T_2$  FSE MR images of rat brains before and after administering the chitosan-coated  $Mg_{1-x}Co_xFe_2O_4$  nanoparticles as contrast agents for  $x = 0.2$  (a),  $x = 0.5$  (b), and  $x = 0.8$  (c). We marked the regions of interest (ROI) 1 and 2 to observe the (%) intensity fall before and after administering the contrast agents for all the values of  $x$ . (d) Fall of intensity at ROI 1 in the brain and ROI 2 in the muscle before and after administering the contrast agents.

ms, 70 ms, 77 ms, 84 ms, 91 ms, 98 ms, 105 ms, and 112 ms. The field of view (FOV) was  $40 \times 40 \text{ mm}^2$ , and the image matrix was  $128 \times 128$ . The transverse relaxation time  $T_2$  is the time of relaxation of net magnetization when it changes by applying a radio-frequency (RF) pulse. Fig. 14(a) presents the  $T_2$  map of phantoms containing chitosan-coated  $Mg_{1-x}Co_xFe_2O_4$  ( $0 \leq x \leq 1$  with  $\Delta x = 0.1$ ) nanoparticles of different concentrations. The darkening effect of each voxel increases with an increase in the concentration for every  $x$  because of the shorter  $T_2$  relaxation time.<sup>28</sup> We found, from the magnetic characterization by Mössbauer and PPMS studies, a transition from the superparamagnetic to the ferromagnetic state with increasing  $x$ . The ferrite nanoparticles accelerate transverse or spin–spin relaxation, which expedites the dephasing of magnetic moments as a consequence of magnetic field gradients generated by the ultrafine magnetic nanoparticles by the subsequent onset of an RF pulse. The spin–spin relaxation is<sup>28</sup>

$$R_2 = \frac{1}{T_2} = \frac{a}{d_{NP}D} \gamma^2 \mu^2 C_{NP} J(\omega, \tau_D) \quad (12)$$

where  $a$  is a constant,  $d_{NP}$  is the nanoparticle diameter,  $D$  is the diffusion coefficient,  $\mu$  is the magnetic moment of the nanoparticles,  $\gamma$  is the gyromagnetic ratio of the water proton,  $C_{NP}$  is the concentration of the nanoparticles, and  $J$  is the spectral density function.

We measured the intensity drop  $I(t)$  with echo time TE. The first-order exponential fitting provides spin–spin relaxation  $1/T_2$  by the relation

$$I(t) = P^* \exp\left(-\frac{t}{T_2}\right) \quad (13)$$

where  $t$  is the decay time,  $P^*$  is the initial intensity, and  $I(t)$  is the peak intensity.<sup>75</sup> From the values of  $R_1 = \frac{1}{T_1}$  and  $R_2 = \frac{1}{T_2}$



relaxation rate with contrast agent of concentration C found from the exponential fitting of eqn (13). The relaxivities of nuclear spins of magnetic nanoparticles in an aqueous solution can be calculated using

$$\frac{1}{T_i} = \frac{1}{T_i^0} + r_i C \quad (14)$$

where  $i$  is 1 or 2,  $\frac{1}{T_i^0}$  is the relaxation rate of the control, and  $r_i$  is the relaxivity of nuclear spins of the nanoparticles (eqn (14)). Fig. 14(b) shows the variations of the relaxation rate with the concentrations. We found a linear relationship between  $1/T_2$  with concentrations of nanoparticles, and the slope gives the values of relaxivities for each  $x$ . Fig. 14(c) shows the variation of  $r_2$  relaxivities with  $x$  because of the change in the magnetic properties with the composition. The obtained values of  $r_2$  relaxivities of chitosan-coated  $Mg_{1-x}Co_xFe_2O_4$  ferrite nanoparticles vary between 15.2 to 185.5  $\text{mM}^{-1} \text{ s}^{-1}$  with  $x$ , which shows almost a linear relationship. Fig. 14(d) shows the variations of the relaxivities with the saturation magnetic moment that shows a linear variation. However the variations of the relaxivity with the initial susceptibility and anisotropy in Fig. 14(e) and (f) are scattered but there is an increasing trend of relaxivity with the susceptibility and anisotropy. Kim *et al.*<sup>30</sup> reported similar results for  $MnFe_2O_4$ ,  $CoFe_2O_4$ , and  $Fe_3O_4$  synthesized by a diol reduction of organic metals. Wang *et al.*<sup>26</sup> reported the  $r_2$  relaxivities of commercially approved MRI phase-contrast agent Ferumoxtran-10 (AMI-227; Combidex, AMAG Pharma; Sinerem, Guerbet), Ferucarbotran (Resovist, Bayer Healthcare), and Ferumoxides (Feridex IV, Berlex Laboratories; and Endorem, Guerbet) as 60, 151, and 98.3, respectively. The  $r_2$  relaxivities are comparable to the relaxivities of chitosan-coated  $Mg_{1-x}Co_xFe_2O_4$  ferrite nanoparticles. Hence,  $Mg_{1-x}Co_xFe_2O_4$  ferrite nanoparticles are potential candidates for the MRI contrast agent.

We acquired the  $T_2$  weighted *in vivo* MRI imaging of the rat brain using the Fast Spin Echo (FSE) pulse sequence. The purpose was to study the efficacy of chitosan-coated  $Mg_{1-x}Co_xFe_2O_4$  nanoparticles. Fig. 15(a-c) shows some representative  $T_2$  FSE MR images of rat brains before and after administering the chitosan-coated  $Mg_{1-x}Co_xFe_2O_4$  nanoparticles as contrast agents for  $x = 0.2, 0.5$ , and  $0.8$ . We marked the region of interest ROI 1 and 2 to observe the (%) intensity drop before and after administering the contrast agents with  $x$ . For instance, at  $x = 0$  and ROI 1, the signal intensity was 17 818 counts for rats before inoculation. The signal dropped to the values of 17 820, 16 578, 10 398, 11 605, and 13 247 counts after 15, 30, 60, 90, and 120 minutes of inoculation of contrast agent. Fig. 15(d) shows the data of (%) intensity fall in the brain (ROI 1) and muscle (ROI 2), which shows the average intensity fall is significant after 60 minutes of inoculation of the contrast agent for the entire range of composition  $Mg_{1-x}Co_xFe_2O_4$  (with  $\Delta x = 0.1$ ). Intensity loss of the  $T_2$  image of rat brain after injecting chitosan-coated  $Mg_{1-x}Co_xFe_2O_4$  nanoparticles varied between 29.2 to 41.6% in Fig. 15(d). Hong *et al.*<sup>27</sup> reported a 31.7% intensity loss in the  $T_2$  image of a rabbit liver after injecting the aqueous solution of chitosan-coated  $Fe_3O_4$ , which supported our result.

## Conclusion

From the FTIR, Raman, and Mössbauer spectra, we observe an increase in cobalt on the tetrahedral site with the increase in  $x$ . Therefore, the addition of cobalt condenses covalent bonds at the tetrahedral site and expands the covalent bonds at the octahedral site. The magnetization increases with  $x$  in the bare condition because of the increase in the A-B interactions and higher magnetic moment of Co. The peak shifts of the absorption bands representing the A- and B-sites of FTIR indicate a good coating with optimum hydrodynamic diameter and zeta potential. The  $T_{\max}$  and SLP of hyperthermia increase with  $x$  due to a higher magnetic moment and anisotropy. The values of  $T_2$  relaxivity,  $r_2$ , increase with  $x$  because of the increase in the magnetic moment, susceptibility, and anisotropy. The *in vivo* studies of rat brain show 29.2 to 41.6% intensity drop after 60 minutes of inoculation of the contrast agent. The present study validates that the chitosan-coated  $Mg_{1-x}Co_xFe_2O_4$  ferrite nanoparticles of all compositions are potential candidates for hyperthermia therapy and MRI contrast. However, the addition of cobalt reduces the concentration of the dose required for hyperthermia therapy and MR imaging.

## Conflicts of interest

There are no conflicts to declare.

## Acknowledgements

The authors would like to offer special thanks to the Annual Development Project (ADP) of the Planning Commission, Government of Bangladesh (the project ID 5003, Nano Project), the Semiconductor Technology Research Centre, University of Dhaka, Ministry of Science and Technology, Bangladesh, and Materials Science Division, Atomic Energy Centre, Dhaka, Bangladesh Atomic Energy Commission for the support to perform this research. The authors are also highly grateful to the International Science Program, Uppsala University, Sweden, for their great support and encouragement.

## References

- 1 A. H. Habib, C. L. Ondeck, P. Chaudhary, M. R. Bock-staller and M. E. McHenry, *J. Appl. Phys.*, 2008, **103**, 07A307.
- 2 A. K. Gupta and M. Gupta, *Biomaterials*, 2005, **26**, 3995–4021.
- 3 M. Arruebo, R. Fernández-Pacheco, M. R. Ibarra and J. Santamaría, *Nano Today*, 2007, **2**, 22–32.
- 4 J. Chomoucka, J. Drbohlavova, D. Huska, V. Adam, R. Kizek and J. Hubalek, *Pharmacol. Res.*, 2010, **62**, 144–149.
- 5 A. Kumar, P. K. Jena, S. Behera, R. F. Lockey, S. Mohapatra and S. Mohapatra, *Nanomedicine*, 2010, **6**, 64–69.
- 6 S. M. Hoque, M. K. Islam, A. Hoq, M. M. Haque, S. Maritim, D. Coman and F. Hayder, *Frontiers in Nanotechnology*, 2021, **3**, 1–13.
- 7 V. K. Sharma, J. Filip, R. Zboril and R. S. Varma, *Chem. Soc. Rev.*, 2015, **44**, 8410–8423.



8 L. A. Frank, G. R. Onzi, A. S. Morawski, A. R. Pohlmann, S. S. Guterres and R. V. Contri, *React. Funct. Polym.*, 2020, **147**, 104459.

9 A. Guerrero-Martínez, J. Pérez-Juste and L. M. Liz-Marzán, *Adv. Mater.*, 2010, **22**, 1182–1195.

10 N. I. Taib, V. Agarwal, N. M. Smith, R. C. Woodward, T. G. S. Pierre and K. S. Iyer, *Mater. Chem. Front.*, 2017, **1**, 2335–2340.

11 J. Simon, L. K. Müller, M. Kokkinopoulou, I. Lieber- wirth, S. Morsbach, K. Landfester and V. Mailänder, *Nanoscale*, 2018, **10**, 10731–10739.

12 S. M. Hoque, M. K. Islam, A. Hoq, M. M. Haque, S. Mar- itim, D. Coman and F. Hyder, *Frontiers in Nanotechnology*, 2021, **3**, 1–13.

13 S. M. Hoque, M. S. Hossain, S. Choudhury, S. Akhter and F. Hyder, *Mater. Lett.*, 2016, **162**, 60–63.

14 M. S. Shakil, M. A. Hasan, M. F. Uddin, A. Islam, A. Nahar, H. Das, M. N. I. Khan, B. P. Dey, B. Rokeya and S. M. Hoque, *ACS Appl. Bio Mater.*, 2020, **3**, 7952–7964.

15 J. T. Tang, X. W. Zeng, Q. S. Xia, X. X. Wang and D. L. Zhao, *J. Alloys Compd.*, 2009, **477**, 739–743.

16 F. Sonvico, S. Mornet, S. Vasseur, C. Dubernet, D. Jaillard, J. Degrouard, J. Hoebeke, E. Duguet, P. Colombo and P. Couvreur, *Bioconjugate Chem.*, 2005, **16**, 1181–1188.

17 L. Khanna and S. K. Tripathi, *Res. J. Recent Sci.*, 2017, **6**, 1–9.

18 H. S. Mund and B. L. Ahuja, *Mater. Res. Bull.*, 2017, **85**, 228–233.

19 F. Cámará-Martos and R. Moreno-Rojas, *Encyclopedia of Food and Health*, 2016, pp. 172–178.

20 US Food and Drug Administration Regulation (FDA), *Food Labeling – Revision of the Nutrition and Supplement Facts Labels (US Food and Drug Administration Regulation) (FDA) (2018 Edition)*, 2018, pp. 903–904, The Law Library, <https://s3.amazonaws.com/public-inspection.federalregister.gov/2016-11867.pdf>.

21 S. Amiri and H. Shokrollahi, *Mater. Sci. Eng., C*, 2013, **33**, 1–8.

22 S. M. Hoque, Y. Huang, E. Cocco, S. Maritim, A. D. Santin, E. M. Shapiro, D. Coman and F. Hyder, *Contrast Media Mol. Imaging*, 2016, **11**, 514–526.

23 T. Yadavalli, H. Jain and G. Chandrasekharan, *AIP Adv.*, 2016, **6**, 55904.

24 A. B. Norman, S. R. Thomas, R. G. Pratt, R. C. Samaratunga and P. R. Sanberg, *Exp. Neurol.*, 1990, **109**, 164–170.

25 P. A. Valdés-Hernández, A. Sumiyoshi, H. Nonaka, R. Haga, E. Aubert-Vásquez, T. Ogawa, Y. Iturria- Medina, J. J. Riera and R. Kawashima, *Front. Neuroinf.*, 2011, **5**, 1–19.

26 Y.-X. J. Wang, *Quant. Imag. Med. Surg.*, 2011, **1**, 35–40.

27 S. Hong, Y. Chang and I. Rhee, *J. Korean Phys. Soc.*, 2010, **56**, 868–873.

28 H. B. Na, I. C. Song and T. Hyeon, *Adv. Mater.*, 2009, **21**, 2133–2148.

29 L. L. Muldoon, S. Gahramanov, X. Li, D. J. Marshall, D. F. Kraemer and E. A. Neuwelt, *Neuro-Oncology*, 2011, **13**(3), 51–60.

30 D. H. Kim, H. Zeng, H. Zeng, T. C. Ng and C. S. Brazela, *J. Magn. Magn. Mater.*, 2009, **321**, 3899–3904.

31 D. Varshney, K. Verma and A. Kumar, *J. Mol. Struct.*, 2011, **1006**, 447–452.

32 M. Y. Lodhi, K. Mahmood, A. Mahmood, H. Malik, M. F. Warsi, I. Shakir, M. Asghar and M. A. Khan, *Curr. Appl. Phys.*, 2014, **14**, 716–720.

33 A. C. Druc, A. I. Borhan, A. Diaconu, A. R. Iordan, G. G. Nedelcu, L. Leontie and M. N. Palamaru, *Ceram. Int.*, 2014, **40**, 13573–13578.

34 M. E. Maguire and J. A. Cowan, *BioMetals*, 2002, **15**, 203–210.

35 M. Barsoum and M. W. Barsoum, *Fundamentals of Ceramics*, Taylor & Francis Group, New York, 2003, vol. 3, pp. 80–84.

36 A. G. Abraham, A. Manikandan, E. Manikandanb, S. Vadivel, S. K. Jaganathan, A. Baykal and P. SriRen- ganathan, *J. Magn. Magn. Mater.*, 2018, **452**, 380–388.

37 C. R. Stein, M. T. S. Bezerra, G. H. A. Holanda, J. André- Filho and P. C. Morais, *AIP Adv.*, 2018, **8**, 056303.

38 J. A. R. Guivar, A. Bustamante, J. Flores, M. M. Santillan, A. M. Osorio, A. I. Martínez, L. D. L. S. Valladares and C. H. W. Barnes, *Hyperfine Interact.*, 2014, **224**, 89–97.

39 Q. Lin, Y. He, J. Xu, J. Lin, Z. Guo and F. Yang, *Nanomaterials*, 2018, **8**, 750.

40 E. Manova, B. Kunev, D. Paneva, I. Mitov, L. Petrov, C. Estournès, C. D'Orléan, J.-L. Rehspringer and M. Kurmoo, *Chem. Mater.*, 2004, **16**, 5689–5696.

41 Y. He, X. Yang, J. Lin, Q. Lin and J. Dong, *J. Nanomater.*, 2015, **2015**, 854840.

42 S. Kumar, A. M. M. Farea, K. M. Batoo, C. G. Lee, B. H. Koo, A. Yousef and A. Y Alimuddin, *Phys. B*, 2008, **403**, 3604–3607.

43 A. Ghasemi, A. Paesano, C. F. C. Machado, S. E. Shirsath, X. Liu and A. Morisako, *J. Appl. Phys.*, 2014, **115**, 17A522.

44 M. Gupta and B. S. Randhawa, *Mater. Chem. Phys.*, 2011, **130**, 513–518.

45 G. A. Sawatzky, F. V. D. Woude and A. H. Morrish, *Phys. Rev.*, 1969, **183**, 383–386.

46 T. Zeeshan, S. Anjum, H. Iqbal and R. Zia, *Mater. Sci.*, 2018, **36**, 255–263.

47 B. Babić-Stojić, V. Jokanović, D. Milivojević, Z. Jagličić, D. Makovec, N. Jović and M. Marinović-Cincović, *J. Nanomater.*, 2013, **2013**, 1–9.

48 R. Vemuria, G. Raju, M. G. Kiran, M. S. N. A. Prasad, E. Rajesh, G. P. Kumar and N. Murali, *Results Phys.*, 2019, **12**, 947–952.

49 I. L. Ardelean, D. Ficai, A. Ficai, G. Nechifor, D. Dragu and C. Bleotu, *UPB Scientific Bulletin, Series B: Chemistry and Materials Science*, 2018, **80**, 33–46.

50 J. Kreisel, G. Lucazeau and H. Vincent, *J. Solid State Chem.*, 1998, **137**, 127–137.

51 P. Galinetto, B. Albini, M. Bini and M. C. Mozzati, <https://www.intechopen.com/chapters/58926>, 2018.

52 H. S. Mund and B. L. Ahuja, *Mater. Res. Bull.*, 2017, **85**, 228–233.

53 M. A. G. Soler, E. C. D. Lima, S. W. da Silva, T. F. O. Melo, A. C. M. Pimenta, J. P. Sinnecker, R. B. Azevedo, V. K. Garg, A. C. Oliveira, M. A. Novak and P. C. Morais, *Langmuir*, 2007, **23**, 9611–9617.

54 K. V. Chandekar, *Adv. Mater. Lett.*, 2017, **8**, 435–443.



55 M. A. G. Solera, T. F. O. Melo, S. W. Silva, E. C. D. Lima, A. C. M. Pimenta, V. K. Garg, A. C. Oliveira and P. C. Morais, *J. Magn. Magn. Mater.*, 2004, 2357–2358.

56 X. Wu, Z. Ding, N. Song, L. Li and W. Wang, *Ceram. Int.*, 2015, **1**, 10.

57 C. O. Ehi-Eromosele, B. I. Ita and E. E. J. Iweala, *J. Sol-Gel Sci. Technol.*, 2015, **76**, 298–308.

58 S. Thota, S. C. Kashyap, S. K. Sharma and V. R. Reddy, *J. Phys. Chem. Solids*, 2016, **91**, 136–144.

59 E. H. M. Sakho, E. Allahyari, O. S. Oluwafemi, S. Thomas and N. Kalarikka, *Thermal and Rheological Measurement Techniques for Nanomaterials Characterization*, Elsevier, 2017, pp. 2–5.

60 M. Zahraei, A. Monshi, D. Shahbazi-Gahrouei, M. Amirmasr, B. Behdadfar and M. Rostami, *J. Nanostruct.*, 2015, **5**, 77–86.

61 M. Arakha, S. Pal, D. Samantarrai, T. K. Panigrahi, B. C. Mallick, K. Pramanik, B. Mallick and S. Jha, *Sci. Rep.*, 2015, **5**, 14813.

62 S. Bhattacharjee, *J. Controlled Release*, 2016, **235**, 337–351.

63 Z. Alborzi, A. Hassanzadeh and M. M. Golzan, *Int. J. Nanosci. Nanotechnol.*, 2012, **8**, 93–98.

64 A. Franco and M. S. Silva, *J. Appl. Phys.*, 2011, **109**, 07B505.

65 M. A. ur Rehman, M. A. Malik, K. Khan and A. Maqsood, *J. Nano Res.*, 2011, **14**, 1–9.

66 E. Pervaiz and I. H. Gul, *Int. J. Curr. Eng. Technol.*, 2012, **2**, 377–387.

67 B. Issa, I. Obaidat, B. Albiss and Y. Haik, *Int. J. Mol. Sci.*, 2013, **14**, 21266–21305.

68 S. M. Hoque, C. Srivastava, N. Venkatesha and K. Chattopadhyay, *IEEE Trans. NanoBioscience*, 2013, **12**, 298–303.

69 E. Grgis, M. M. S. Wahsh, A. G. M. Othman, L. Bandhu and K. V. Rao, *Nanoscale Res. Lett.*, 2011, **6**, 460.

70 A. Franco and F. C. e Silva, *Appl. Phys. Lett.*, 2010, **96**, 172505.

71 E. U. Okon, G. Hammed, P. A. E. Wafa, O. Abraham, N. Case and E. Henry, *Int. J. Innovation Appl. Stud.*, 2014, **5**, 192–199.

72 A. K. Veni and S. Mohandass, *International Journal of Pharmacognosy and Phytochemical Research*, 2014, **6**, 320–323.

73 P. W. Prasetyaningrum, A. Bahtiar and H. Hayun, *Sci. Pharm.*, 2018, **86**, 25.

74 J. H. Lee, J. Jang, J. Choi, S. H. Moon, S. Noh, J. Kim, J. G. Kim, I. S. Kim, K. I. Park and J. Cheon, *Nat. Nanotechnol.*, 2011, **6**, 418–422.

75 H. M. Joshi, Y. P. Lin, M. Aslam, P. V. Prasad, E. A. Schultz-Sikma, R. Edelman, T. Meade and V. P. Dravid, *J. Phys. Chem. C*, 2009, **113**, 17761–17767.

